nature communications

Article

https://doi.org/10.1038/s41467-025-60982-0

Modular shape-changing tensegrity-blocks enable self-assembling robotic structures

Received: 25 November 2024

Accepted: 6 June 2025

Published online: 01 July 2025

Check for updates

Luyang Zhao[1] ✉, Yitao Jiang[1], Muhao Chen[2], Kostas Bekris[3] & Devin Balkcom[1]

Modular robots are currently designed to perform a variety of tasks, primarily focusing on locomotion or manipulation through the reconfiguration of rigid modules. However, the potential to integrate multiple functions, such as making each robot deployable and capable of building lattice structures for self-construction and infrastructure creation, remains largely unexplored. To advance the field, we hypothesize that combining tensegrity principles with modular robotics can create lightweight, deformable units capable of integrating three critical functions within a single design: navigating varied terrains, manipulating arbitrary shape objects, and assembling weight-sustainable, active large infrastructures. Here, we designed untethered modular robots that are deformable, lightweight, deployable, outdoor-scale, capable of bearing loads, and capable of 3D attachment and detachment. With these characteristics, the system can form various 3D structures using different assembly methods, such as walking into position or being transported by rotorcraft. The deformability and lightweight nature of each block enable the assembled structures to dynamically change shape, providing capabilities such as added compliance during locomotion and manipulation and the ability to interact with the environment in tasks like tent and bridge assemblies. In summary, we suggest that integrating lightweight and deformable properties into modular robot design offers potential improvements in their adaptability and multi-functionality.

Traditional robots are normally highly specialized and effective in controlled environments, designed for specific tasks that require precision, repeatability, and reliability[1]. However, in emergency situations, there is a pressing need for robotic systems that are not only versatile but also quickly deployable to address a wide range of challenges. These scenarios often require the rapid assembly of temporary structures, such as antennas, scaffolding, and shelters, as well as the deployment of robots capable of navigating and transporting supplies across unstructured terrain. Drawing inspiration from the capabilities of biological insects, such as army ants (*Eciton* genus), which link their bodies to form bridges across gaps in their foraging paths[2], and fire ants (*Solenopsis invicta*), which form rafts to survive floods[3], researchers have developed modular robots that, though still at the proof-of-concept stage, present several potential advantages. Currently, these robots can adapt to various tasks through reconfiguration and are reusable across different missions, often built with rigid modules with a focus on one or two specific functions, such as locomotion or manipulation[4–6]. Recent designs, such as SMORES[7,8], Sambot[9], showcase how those untethered, self-assembling, rigid modular robots can reconfigure into different configurations to achieve various locomotion patterns. Multi-legged robot swarms[10] successfully incorporated appendages such as limbs into the robot design and showed the capabilities of modular robots to navigate rough outdoor terrains. While modular robotic systems have mainly

[1]Department of Computer Science, Dartmouth College, Hanover, NH, USA. [2]Department of Mechanical and Aerospace Engineering, University of Kentucky, Lexington, KY, USA. [3]Department of Computer Science, Rutgers University, New Brunswick, NJ, USA. ✉e-mail: luyang.zhao.gr@dartmouth.edu

focused on locomotion[6,11], there are a few examples of systems that attack manipulation, either using grippers formed from the modules[11], turning a screw with aerial rotorcraft[12], or transporting a table by lifting[13]. Despite these advances, a significant gap remains in creating modular robots that are not only adaptable for locomotion and manipulation functions but also easily deployable, packable, and capable of constructing temporary structures on a human scale.

To address this gap, tensegrity structures[14,15], known for their lightweight design, can sustain significant weight while also being able to deform and adapt to different shapes, making them an ideal complement to modular robotic systems that require both versatility and robustness. They typically consist of rigid components, such as rods, held together by flexible elements like cables or strings, allowing them to be both lightweight and compliant[14]. NASA's Super Ball Bot exemplifies the potential of active tensegrity robots, utilizing cable-driven systems for both landing and locomotion[16]. Research studies on pre-assembled tethered module-based tensegrity robots have also demonstrated their effectiveness in outdoor locomotion and as robotic grippers[17,18], further highlighting the practical applications of these structures. Moreover, the lightweight and deformable properties that are crucial to our design enable efficient transport and deployment via rotorcraft with very limited loading capacities, representing an early but important step toward the development of flexible, rapidly deployable robotic solutions for various applications, including emergency response.

Untethered operation is also crucial for making each module more practical. Small-sized, shape-changing soft modular robots primarily use three actuation methods. The first is high-current Shape Memory Alloys (SMAs), which allow for quick demonstrations but are difficult to design for untethered use, making outdoor testing challenging[17,19]. Despite this limitation, tethered shape-changing soft modular robots actuated by SMAs excel in manipulation through deformation, whereas rigid robots often need extra parts to achieve similar functionality[6,20]. Pneumatic systems, such as air pumps, also struggle with the untethered operation, though Foambot[21] manages untethered vibration using an air pump. A more complex but effective approach is cable-driven systems, which adjust string lengths via motor-pulley mechanisms, offering broader control bandwidth, lower cost, and greater environmental robustness. Eciton Robotica[22] demonstrates untethered operation using this method, showcasing soft modular robots capable of self-assembling. However, fully adaptable, deformable, untethered soft modular robots face ongoing challenges such as self-recognition, module communication, and the complexities of assembly and disassembly[11], which need to be addressed for practical deployment in unstructured environments.

Scaling up soft modular robots to human size is beneficial for making them applicable in people-centric and outdoor applications. Some manually assembled modular flexible systems offer meter-scale solutions, such as legged locomotion across various terrains via shape-changing capabilities[23–25]. Achieving self-assembly allows for more complex, responsive behaviors, requiring durability in diverse environments and the ability to autonomously navigate and interact with complex terrain. This scale-up also unlocks possibilities for constructing human-scale infrastructure, such as shelters and bridges. Although the use of active modular robots for human-sized infrastructure construction remains largely unexplored, promising advancements in related fields highlight its potential. For example, passive structures have been successfully assembled using mobile robots and aerial rotorcraft, such as the construction of a 6-meter-tall tower from 1500 foam blocks by quadcopter[26–29]. Our work explores the integration of active modular blocks into rotorcraft-assisted construction, with the goal of enabling the formation of active 3D structures, such as active scaffolding equipped with an antenna that can dynamically adjust to point toward a satellite to increase signal reception.

In this work, we have integrated the properties of modular and tensegrity robots to create a system that embodies five key characteristics essential for each module: (a) lightweight and easily deployable, (b) deformable, (c) untethered operation, (d) designed for outdoor use and capable of bearing loads, and (e) capable of 3D attachment and detachment. With these characteristics, our system can form various 3D structures using different assembly methods, such as walking into position or being transported by rotorcraft. The deformability of each block allows assembled structures to dynamically change shape, while the lightweight nature enables the blocks to be deployable by rotorcraft. These capabilities allow the modules to achieve three distinct functions (Fig. 1): (i) effective locomotion across different terrains by adapting their shape, (ii) versatile object manipulation through various methods (grasping and non-prehensile manipulation), and (iii) rotorcraft-assisted assembly into active 3D lattice structures. These functions are not isolated; rather, they interact synergistically, allowing an assembled active structure to potentially perform multiple tasks through whole-body deformation, with the potential to interact adaptively with humans and the environment without requiring reassembly. For example, a snake-like configuration of blocks can move through open spaces, contract to navigate narrow openings, and transport objects along its path. A chain of blocks can form a bridge over a gap by locomotion, with the active bridge also capable of undulating to transport objects across. A human-scale shelter skeleton can be lowered to facilitate fabric placement and then raised to its full height. These examples showcase the versatility and potential of active structures.

Results

Robot design and characteristics

To meet diverse functional requirements, especially for block deployment and 3D structure formation, we opted for a simple, cubic design for each block, as its symmetrical properties facilitate tiling into larger structures using axis-aligned connectors, reducing the complexity of assembly. Figure 1 illustrates the physical design of a single block, which differs from traditional tensegrity robots like the well-known 3-bar or 6-bar designs, where rods are connected solely by strings or cables. Each block in our design features a flexible central joint (TPU printed), which behaves similarly to a ball joint, from which eight rigid rods extend outward in a 3D radial pattern, classifying it as a class-8 tensegrity structure according to *Tensegrity Systems* by Skelton and De Oliveira[14]. Each rod terminates in an endcap, with the twelve adjacent pairs of endcaps connected by strings that can be adjusted in length by motors housed within the endcaps. This 3D rotational symmetry across various axes allows for the connection of adjacent blocks in multiple orientations, enabling versatile assembly configurations.

Aiming to achieve untethered operation, all 12 actuators and 12 connectors are integrated into the 8 endcaps, and each block is powered by an onboard Lithium-ion battery capable of supporting locomotion on flat ground for up to 3.5 h. A customized PCB includes onboard sensing components comprising an Inertial Measurement Unit (IMU), a Wi-Fi module, and an RP2040 microcontroller for twelve-channel encoder processing.

With the focus of creating a lightweight, easily deployable, and outdoor-capable module with a relatively good thumb of load-bearing capacity, we used carbon fiber bars and high-stiffness strings in the design. This choice of carbon fiber enables each module to weigh less than 1.2 kg, with dimensions of 52.11 cm per side length, resulting in a density of 8.53 kg/m^3. The blocks are also designed to withstand drops of up to 3 m onto various outdoor surfaces without damage (Movie S12), ensuring robustness during rotorcraft-assisted vertical assembly. Each module can support a load of approximately 153.53 N, demonstrating a load-bearing capacity of 13 times its own weight. Additionally, similar to the approach taken for AuxBots[30], we also tested the actuated lifting forces, finding that our blocks can exert

forces 7–11.5 times their own weight (AuxBots can exert forces 23–76 times their weight). Failures typically occur in the carbon fiber rods. Depending on the specific applications, design adjustments such as using thicker rods or strings may be required for enhanced load-bearing capacity or drop resistance, or employing longer rods for larger-scale module designs.

Each cable is actuated by a motor that adjusts its length. The motor is secured by a holder on the inner side of the endcap, as shown in Fig. 2d. A winch attached to the motor winds the cable, which passes through a hole in the endcap and connects to a tie point on the opposite endcap. In the initial state, all strings have the same length and are under equal tension. During actuation, we apply different power levels to individual motors depending on whether each string is being contracted or extended. Specifically, when a motor is used to contract a string, it operates at a higher power level (e.g., 100%) to generate sufficient pulling force. Conversely, when a motor is releasing

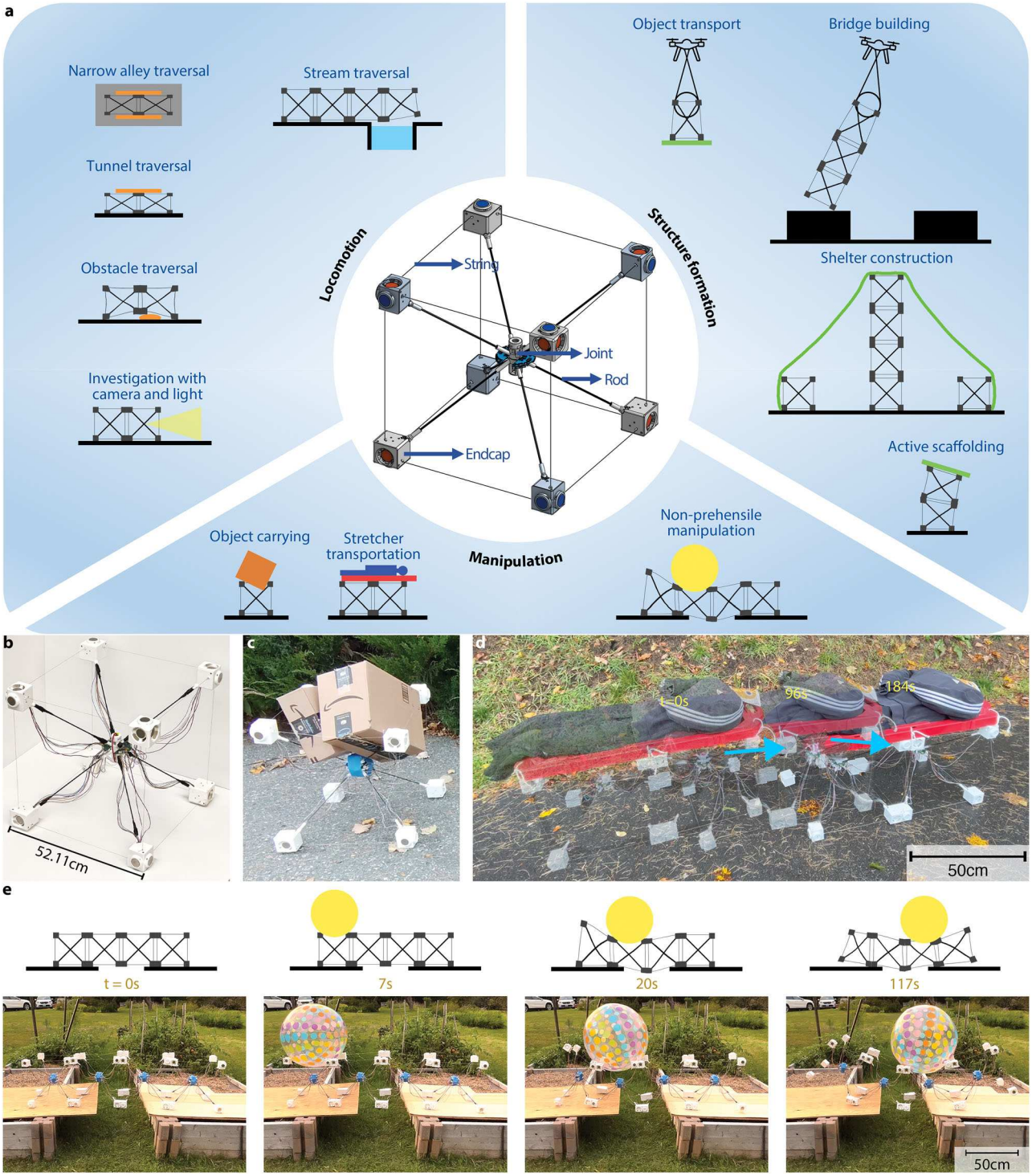

Fig. 1 | Robot capabilities and examples. a System capabilities include locomotion over various terrains and obstacles, manipulation, such as stretcher transportation, as well as structure formation. **b** A single block. **c** Object carrying. **d** Time-lapse transportation of a stretcher mock-up on blacktop. **e** Whole-body wave-like motion transferring a ball.

https://doi.org/10.1038/s41467-025-60982-0

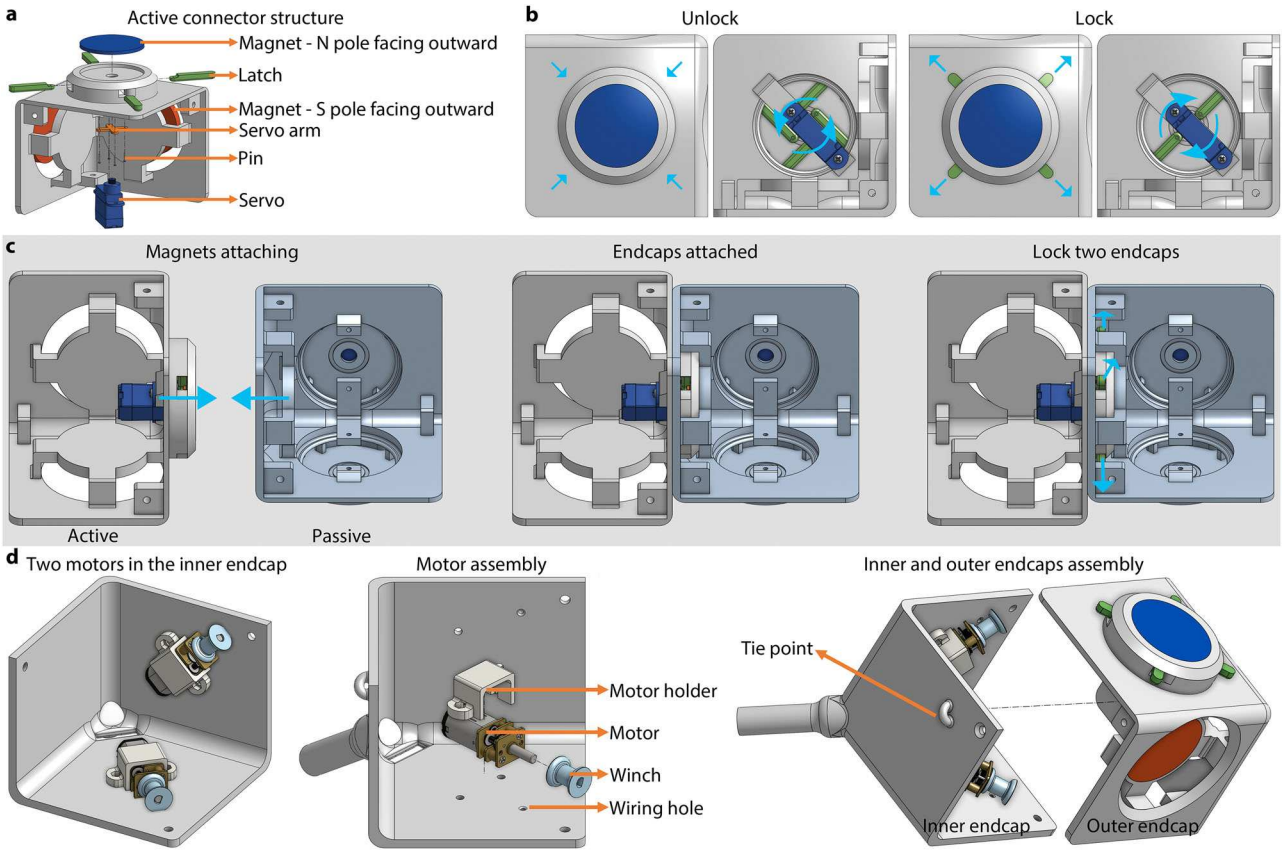

Fig. 2 | Endcap design and attachment. a Exploded-view drawing of the active connector. **b** Two states of the active connector: unlocked, with latches rotated inward, and locked, with latches rotated outward. **c** Magnetic alignment to attach and the mechanical lock process. **d** Motor assembly and the endcap assembly.

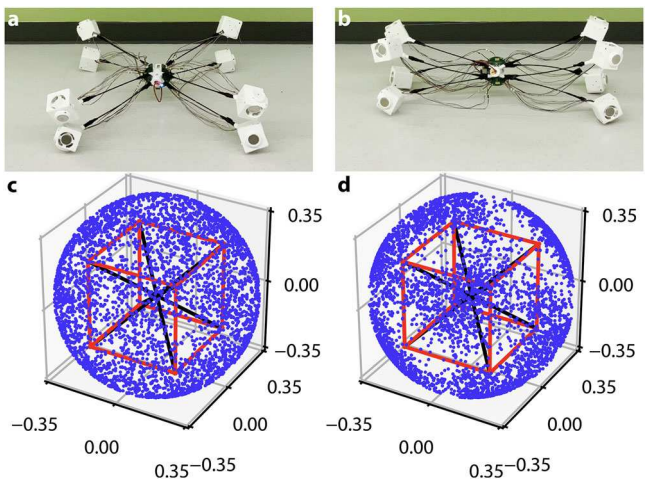

Fig. 3 | Two packing strategies and the workspace of a single module subject to different minimum string lengths. a Flattened shape. **b** Bundle shape. **c** Workspace of a single module when min string length equal to 0, (**d**) and 0.5*l*.

a string, it applies a lower power level (e.g., 80%) to maintain control while reducing unnecessary slack. The power level thus reflects both the desired speed and force applied to each string. This strategy helps maintain consistent tension across all strings during deformation. When the robot is static, the motor gearboxes provide a self-locking force that prevents unintended structural deformation.

Flexible central joints and 12 adjustable-length cables (actuated by 12 motors) enable the structure to adapt to various configurations. For instance, shortening four parallel strings while accordingly extending the other eight strings compacts the robot into a flattened shape, reducing its height to 30% (Fig. 3a, Movie S11), while shortening eight strings (extending the other four correspondingly) on two parallel faces compresses it further into a bundle, reducing its volume to 41% of its original size (Fig. 3b, Movie S11). Additionally, four strings on a single face can be shortened to perform a gripping action on external objects. By actuating strings in specific sequences, the robot can also achieve continuous motions to achieve locomotion. To achieve a desired configuration, the controlled string lengths can be determined by solving the nonlinear static equation, $\boldsymbol{Kn} = \boldsymbol{f}_{ex} - \boldsymbol{g}$, using the Lagrangian method described in ref. 31. In this equation, $\boldsymbol{K}$ represents the stiffness matrix, $\boldsymbol{n}$ the nodal coordinates, $\boldsymbol{f}_{ex}$ the external force matrix, and $\boldsymbol{g}$ the gravitational force matrix. Using the matrix-based form-finding method[32] to solve the static equation allows us to determine all feasible shapes within the robot's workspace. The workspace for string movements from 0 to l (initial length of the string between two endcaps) and from 0.5l to l is depicted in Fig. 3c, d, respectively, based on 500 samples. These deformation capabilities allow each robot to not only locomote but also be packed into a compact form for transport and function as a gripper for object manipulation. To further assess whether the deformation is primarily due to the central joint or if the rods also bend, we conducted experiments measuring the displacement versus force relationship for a single carbon fiber rod, both with and without the central joint. The results show that achieving a 5 cm displacement required approximately 0.5 N with the central joint, compared to 12.8 N for the rod alone (Fig. S5). The results indicate that the deformation is primarily due to the central joint, as the rods exhibit significantly higher stiffness and resistance to bending.

For the purpose of enabling robust 3D structure formation, self-assembly, and self-disassembly, we require the connectors between

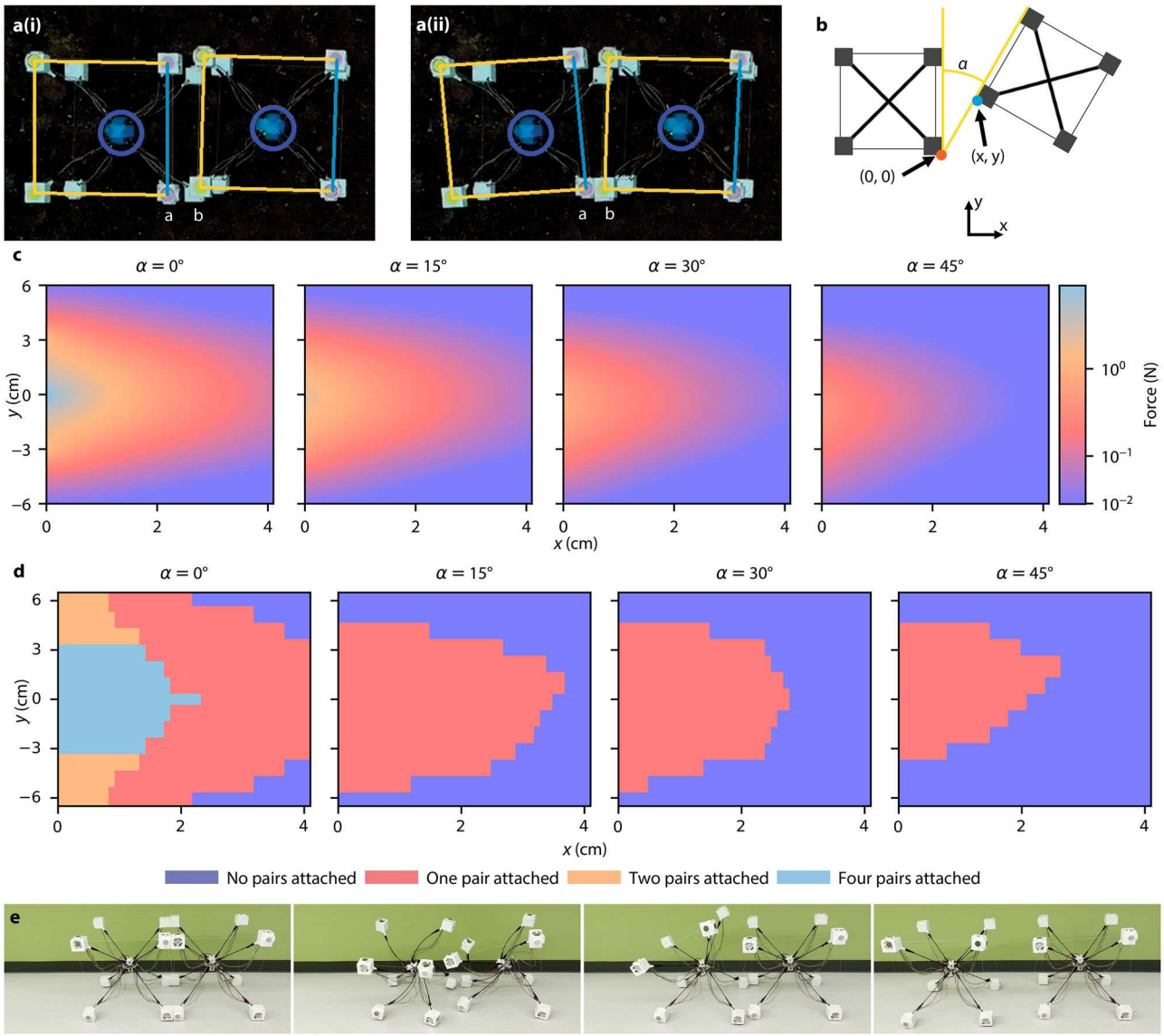

Fig. 4 | Attachment and detachment. a State estimation and detection of attachment. **a(i)** The state when no endcaps between two blocks are attached, where the image distance between endcaps a and b is 49.2 pixels. **a(ii)** The state where a pair of endcaps (a and b) are attached. The distance between these two endcaps is 27 pixels, which falls below the defined threshold of 35 pixels. We consider two endcaps attached when their distance is less than this threshold. **b** Alignment experiment setup for a pair of blocks at different configurations. **c** The magnetic forces between two endcaps at varied distances and angles of 0°, 15°, 30°, and 45°. **d** Alignment robustness contour for a pair of blocks at different configurations. **e** Detachment between two modules.

blocks to have four properties: secure connection, error-tolerant attachment, reliable detachment, and power efficiency. Due to the lack of inherent mobility of each individual unit, most existing shape-changing modular robotic systems either depend entirely on manual assembly[23,33–39] or partially[21,40,41]. In addition, permanent magnets are commonly employed for connection[19,20,42], but strong magnets are difficult to separate for detachment. Additionally, the larger the robot, the larger and more impractical the required magnets become. Electromagnets[43] and electro-permanent magnets[44] have been used in rigid modular robots but require heavy coils or substantial electrical current.

In pursuit of the four desired properties, we designed the connector (Fig. 2) with four specific features, each tailored to meet one of our requirements. First, the connector incorporates a mechanically interlocking design that sustains at least 370 N of force per pair of endcaps, ensuring a secure connection that can withstand loads at least 125 times the robot's weight. Second, permanent magnets are included to mitigate alignment errors, contributing to error-tolerant attachment. Third, the connector allows for reliable detachment through the combination of the first two designs that facilitates easy separation when necessary. Lastly, the connector operates with low power consumption, requiring about 0.06 J of energy per connection via a latch-servo mechanism, and once locked, it does not require additional power to maintain the connection. To evaluate the effectiveness of the magnetic alignment, we conducted experiments by fixing one block's position and placing another at various angles (0, 15, 30, 45, and 60 degrees) and distances at 1 cm intervals (Fig. 4b). Our results, shown in Fig. 4d, indicate that at angles of 45 degrees or less, at least one pair of endcaps attaches, enabling further movement toward complete docking. However, at 60 degrees, no attachment is observed. The magnetic force between a pair of endcaps (Fig. 4(a(ii)), endcaps a and b) on two modules is shown in Fig. 4c, with the model used for calculation described in the "Supplementary Methods" section.

Specific gaits are developed for both the docking and undocking processes. For docking, we designed two specific gaits:

turn_left_fix_vertical_left_front and *turn_left_fix_vertical_left_back*. Testing these gaits demonstrated that even when only one pair of endcaps initially makes contact, the appropriate gait ensures the successful attachment of the remaining endcap pairs, resulting in 10 successful attachments out of 10 trials. For undocking, an unscrewing motion is employed. This process begins with the shortening of the horizontal strings on the first module and the vertical strings on the second module, followed by reversing the sequence: shortening the vertical strings on the first module and the horizontal strings on the second module (Fig. 4e, Movie S11)).

Structure formation

What kinds of active structures can our module design achieve? This section demonstrates several possibilities, including bridges that enable non-prehensile manipulation, tents that expand or contract for use and disassembly, and scaffolding that can rotate to direct an antenna or solar panel.

Rotorcraft plays a key role in the demonstrated deployment, vertical assembly, and provides camera perception. For deployment, the rotorcraft must have a payload capacity exceeding the weight of the module; our modules weigh 1.2 kg, while the DJI Matrice 350 RTK rotorcraft used in this study has a payload capacity of 2.7 kg. The size of the rotorcraft (unfolded, without propellers) is similar to that of one module: 81 cm × 67 cm × 43 cm (L × W × H) compared to 52.1 cm × 52.1 cm × 52.1 cm. We tested the flight duration, which was about 30 min, imposing a constraint on extended assembly tasks.

Terrestrial formation of structures: block connection. The structure formation on land involves attaching pairs of blocks, where one block remains stationary while the other, the active block, selects gaits from predefined gait primitives generated by the *gait generation helper* to approach the target. This attachment process consists of two critical phases: the *approach* phase, guided by real-time motion planning and low-level re-planning to mitigate errors, and the *connection* phase, where blocks are precisely aligned and joined. The transition between these phases is determined by the distance and angular differences between the start and goal positions of the active block. If the start and goal are within a threshold of 350 pixels (a unit derived from image-based sensing) and 10 degrees, the process advances to the second phase; otherwise, it continues refining the *approach* phase until proximity is achieved.

To ensure accurate real-time sensing during both phases, we employ a rotorcraft-mounted camera to provide a broad field of view and enable rapid repositioning for large modules. Hovering at 4.5 meters, the rotorcraft detects color-coded fiducials—blue for the middle joint and pink/yellow for endcaps—on each block. To estimate the state of each block, we first identify white endcaps via brightness thresholding, establishing boundaries for the colored fiducials. Color detection is then performed within predefined HSV ranges, adjusted for lighting variations. We select $4n$ regions optimized for the desired area-to-perimeter ratio, where n is the number of visible modules. Finally, a global distance minimization algorithm associates each blue joint with its closest color fiducials, allowing precise calculation of each module's position (x, y) and orientation (θ). The system operates with a latency of approximately one second, primarily due to image data transmission.

In the *approach* phase, an A* search algorithm is used to find a path to the goal using five selected gait primitives. The modules' symmetrical design, lacking a defined front, left, right, or back, allows any side to act as the 'front,' facilitating directional changes. To reduce the search space, a 'front' face is defined based on the color fiducial on each module, with active modules consistently using the left face to connect with passive robots. This simplification, however, comes with a cost— in tight spaces, it may be beneficial to use motions outside this limited set of primitives. Nonetheless, these primitives have been sufficient for the demonstrated examples. We set a maximum of 10,000 iterations for the A* algorithm. If A* fails due to overly tight constraints on reaching the goal, the blocks continue with the gait from the last successful search. If there is no recent path, the blocks use a greedy algorithm to choose the action that most decreases the distance to the goal. The primitives used by A* include *turn_left*, *turn_right*, *turn_slow_left*, *turn_slow_right*, and *slide_left_slow*.

In the *connect* phase, the active module employs three sliding mechanisms to make the final approach: *slide_left_slow*, *slide_left_slow_front_more*, and *slide_left_slow_back_more*. When the absolute angular difference between the active and passive modules is large, *slide_left_slow_back_more* is selected if the active module has a larger angular value; otherwise, *slide_left_slow_front_more* is used. When the angular difference is small, the module typically chooses *slide_left_slow*. However, to avoid the possibility of the *slide_left_slow* primitive becoming stuck on a terrain obstacle, there is a small probability that the module randomly selects one of the other two primitives, as shown in the data collected (Fig. S2).

To verify whether a connection is successfully established between two modules, we employed a vision-based method to monitor the distance between the corresponding endcaps. In particular, we analyze whether the two visible endcaps on each module are within a threshold distance, indicating a successful mechanical connection. For example, in Fig. 4a(i), endcaps *a* and *b* are detected as not attached, whereas in Fig. 4a(ii), they are recognized as attached. From repeated trials, we established an empirical threshold of 35 pixels based on image-based distance estimation to determine attachment status. Once both pairs of endcaps between two modules are confirmed to be connected, the system marks the self-assembly between these modules as complete. Additionally, we observed that when the top endcaps connect, the bottom endcaps typically align and attach automatically due to the structural constraints, which is why only the top endcaps are color-coded and monitored using the overhead camera.

To showcase both the system's capabilities in structure formation and its ability to rescue malfunctioning robots, we present an example of a rescue scenario involving a damaged block (see Fig. 5 and Movie S1). In this scenario, the far-left block is broken, and the other two blocks act to rescue it. Figure 5b shows the side and top views of the blocks, highlighting their automatically planned movement trajectories. The first rescue block attaches to the broken block (0 s–164 s). Since the malfunctioning block lacks power, only the active connectors on the rescue block are actuated during attachment, resulting in only two pairs of endcaps being connected. The second rescue block then joins (186 s–1387 s), and together they pull the broken block to safety (1446 s–1736 s).

Aerial formation of structures: vertical lifting and assembly. To use rotorcraft for vertical assembly, the block grasping mechanism was designed to avoid interfering with the rotorcraft's landing. The mechanism needed to be compliant to handle the challenges posed by wind conditions, which make precise docking difficult. A cable and inflated ball mechanism was developed and attached to the rotorcraft. The rotorcraft positions the ball on top of the block, which then grasps the ball for secure flight. For terrestrial connections, the sensing, planning, and execution loop automates module connections. However, the 1-s latency in the vision system complicates dynamic aerial connections. As a result, the examples in this section were demonstrated using human remote control of the rotorcraft. During teleoperated assembly, the modules themselves do not execute specific motion patterns to assist in connection. Instead, the human operator manually aligns the modules by first attaching one pair of endcaps, followed by a nearby pair. Once two or three pairs of endcaps are connected, the fourth pair typically attaches automatically due to the embedded magnets.

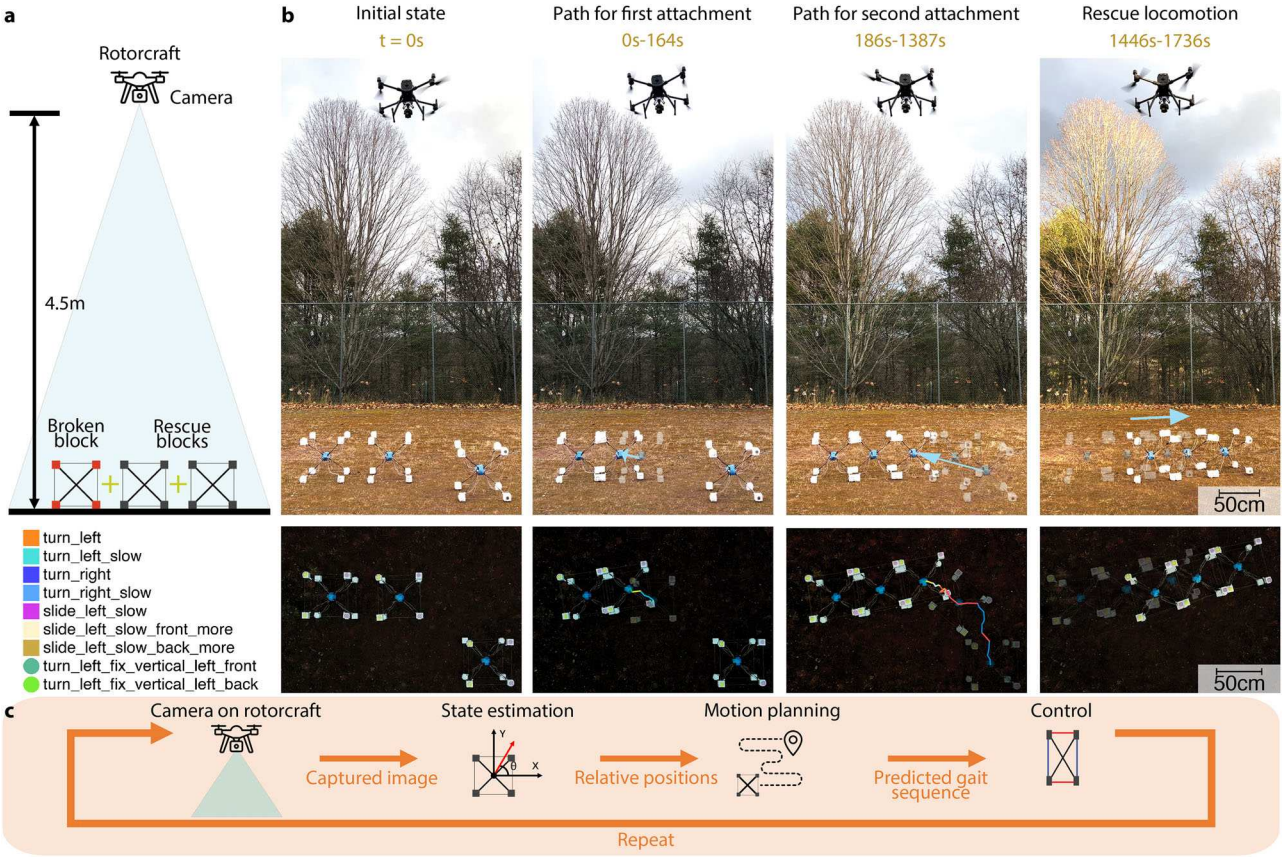

Fig. 5 | Planning and control. a A rotorcraft hovers at 4.5 m. Below, three blocks are positioned: one malfunctioning block on the left and two rescue blocks. **b** Side and top views of initial block positions and movement. **c** Operational workflow: on-board control, off-board state estimation, and motion planning.

Figure 6 shows several examples of how 3D structures, such as tents, adaptive scaffolding, and bridges, can be assembled using a rotorcraft. Figure 6a and Movie S4 show a rotorcraft constructing adaptive scaffolding that provides targetable support for solar panels. Once blocks have been assembled into a scaffolding tower, a block then grasps the solar panel and lifts it to position; the tower can then deform to track the sun. Figure 6b and Movie S5 show an example of forming a bridge. First, blocks are assembled into a vertical stack on one island; the rotorcraft then tilts the stack to form the bridge. Figure 6c and Movie S3 show the construction of a shelter from nine blocks on fairly level grass. The rotorcraft assembles a 2-m tall structure and delivers the 3 kg fabric. Then, the shelter compresses to be short enough (about 70%) that a human can attach the fabric.

To evaluate the structural stability under varying loads, we analyzed the critical buckling load, which is defined as the load at which a structure is susceptible to global buckling. This critical load was determined by solving the generalized eigenvalue problem for the scalar α, as expressed in the following equation: $-(\boldsymbol{K}_{G2} + \boldsymbol{K}_E)\,\mathrm{d}\boldsymbol{n} = \alpha \boldsymbol{K}_{G1}\mathrm{d}\boldsymbol{n}$, where $\boldsymbol{K}_{G1}$ and $\boldsymbol{K}_{G2}$ represent the geometric stiffness matrices due to external loading and prestress, respectively, and $\boldsymbol{K}_E$ denotes the material stiffness matrix[45]. Using this formulation, we computed the critical buckling compressive loads for various structural configurations. As illustrated in Fig. 7, a single-unit configuration exhibited a critical buckling load of 179.07 N. For horizontally combined configurations of two, three, and four units, the critical loads were calculated to be 286.06 N, 286.21 N, and 286.06 N, respectively. Horizontal bridge configurations comprising three and four units demonstrated loading capacities of 187.58 N and 295.85 N, respectively. In contrast, vertically combined units exhibited slightly lower critical loads, with values of 176.83 N, 176.24 N, and 175.93 N for two, three, and four units, respectively. Additionally, the critical buckling load for a tent structure was determined to be 202.59 N. Experimental validation for a single unit under compressive load resulted in a measured critical load of 153.53 N, closely approximating the predicted value of 179.07 N. The observed discrepancy can be primarily attributed to imperfections in the structural bars, strings, and 3D-printed joints. Moreover, the eigenvalues of the stiffness matrices for the ten structural configurations are provided in Fig. 7.

Manipulation

A primate may grasp a tool tightly to manipulate it[46]. A dolphin playing with a ball employs a *whole-body* non-prehensile approach to manipulation[47]. Ants perform cooperative transport by synchronizing individual actions with the group's collective force[48]. Different arrangements of robotic blocks and tasks motivate the use of each of these strategies. In this way, the developed system provides a platform for exploring different types of manipulation.

A single module is capable of functioning like a gripper (Fig. 6). This capability is demonstrated in rotorcraft deployment, where a block acts as a gripper to hold onto a ball mounted on the rotorcraft. Apart from the ball, the module can grip additional robots, boards, fabric, or balls. This also enables autonomous construction of active structures, similar to how prior rotorcraft systems have constructed passive architectural structures[28,29]. We investigate the gripping mechanics based on the geometric contact of the carbon fiber and endcap with the object. Our analysis reveals two contact phases depending on the object's diameter: for objects larger than 212.5 mm, the carbon fiber rods make contact with the object, and the endcap vertices attach to the object. For smaller objects, the endcap edge is tangent to the object. The contact angle on the endcap determines holding and gripping forces. The contact angle ranges from 90° (for objects near the module's maximum size) down to lower angles as the

https://doi.org/10.1038/s41467-025-60982-0

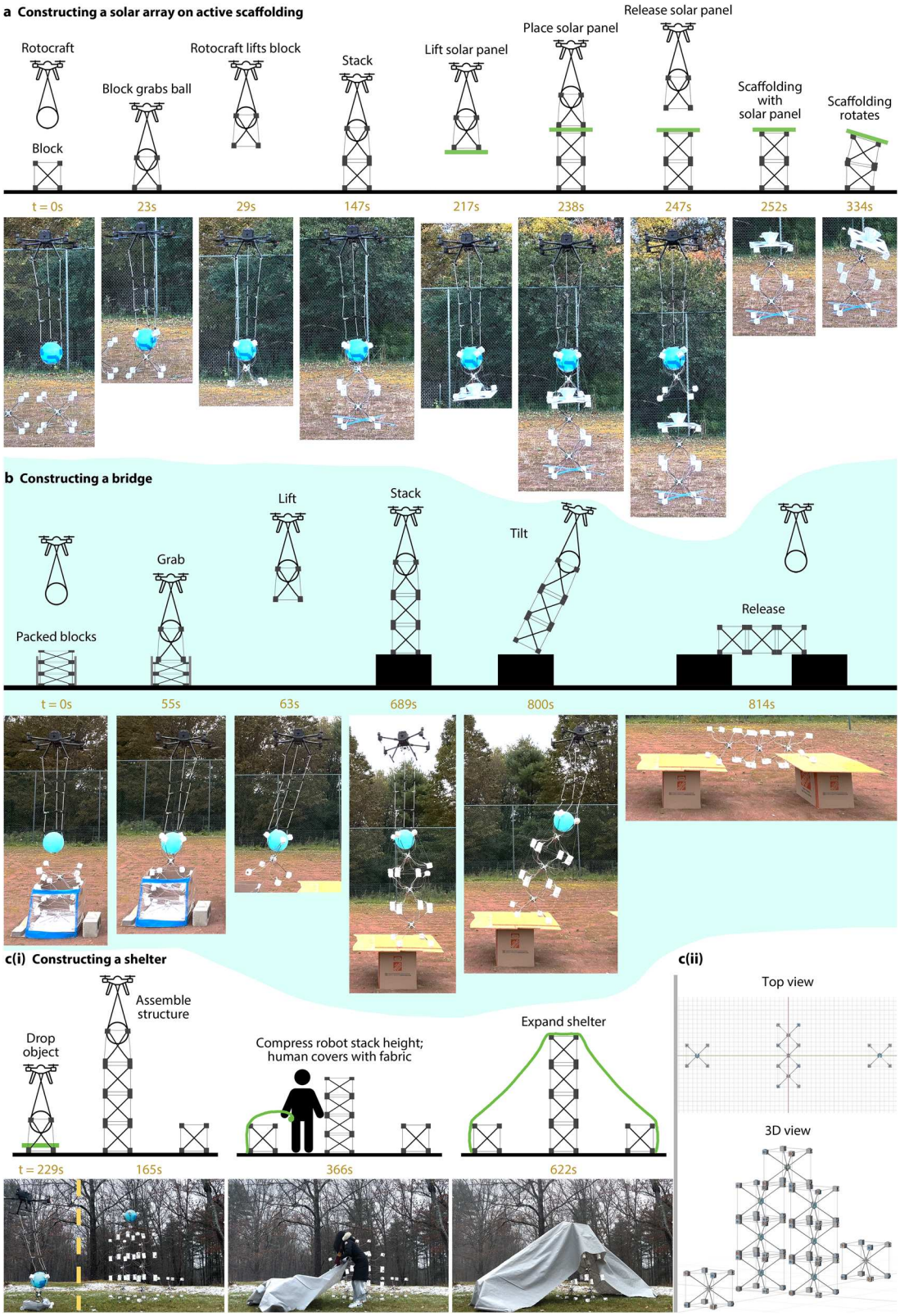

Fig. 6 | Structure formation with rotorcraft assistance. a Adaptive scaffolding formation: block-rotorcraft pair transports the block (t = 23 s), assembles the structure (t = 147 s), and deploys a solar panel (t = 238 s–247 s), with the completed scaffolding rotating up to 360 degrees. **b** Rotorcraft-assisted bridge formation: modules start in a box (t = 0 s), the rotorcraft forms blocks into a vertical structure (t = 63 s), tilts the structure (t = 800 s), and completes a bridge over a 2-block width gap (t = 814 s). **c (i)** Rotorcraft aiding in tent skeleton assembly (t = 165 s), dropping a block with covering cloth (t = 229 s), and tent completion with the stretched skeleton (t = 366 s). **(ii)** Top and 3D views of the block-based tent skeleton.

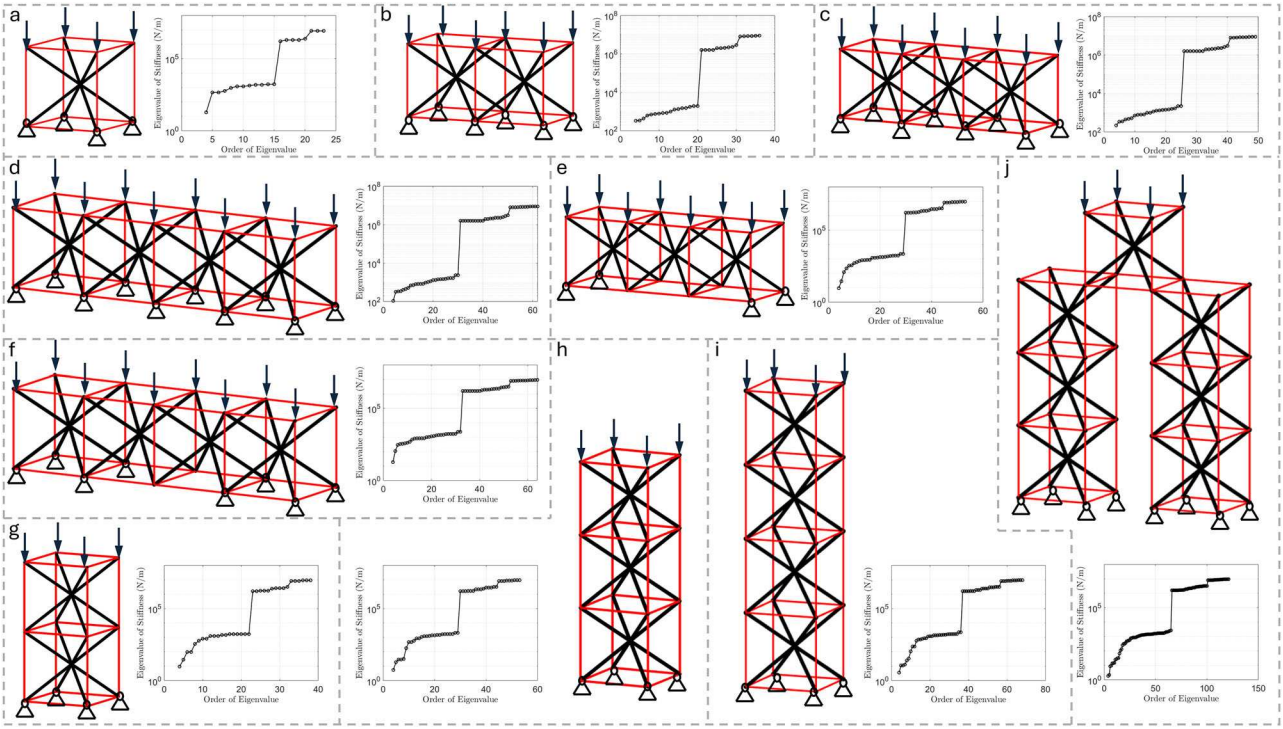

Fig. 7 | Various structural configurations and stiffness plots. a Single unit. **b** Two horizontally connected units. **c** Three horizontally connected units. **d** Four horizontally connected units. **e** A bridge: three horizontal units with fewer ground supports. **f** A 4-bridge. **g** Two vertically stacked units. **h** Three vertically stacked units. **i** Four vertically stacked units. **j** Tent structure.

object size decreases. Based on motor torque and contact geometry, the theoretical maximum tension is approximately 425 N, but structural failure occurs around 150 N in practice. These insights inform both hardware limits and safe operating ranges. More details are provided in the "Supplementary Methods" Contact mechanics and holding force analysis.

To demonstrate the potential of modular robots for transporting objects, similar to warehouse robots such as those developed by Kiva Systems—Amazon Robotics[49], which transport shelving units, we present the following examples. As illustrated in Fig. 1c, a single block can transport two boxes. Further, Fig. 1d and Movie S9 show a pair of blocks transporting a manikin on a stretcher. The manikin used, along with the stretcher, weighs approximately 5 kg, which is significantly lighter than an average human. While the current blocks are neither strong enough to carry a human nor fast enough for emergency response, with further fine-tuning to improve their weight-sustaining capability, they have the potential to be used for transporting heavier objects in the future. To enable the system to sustain human-weight loads, four key factors must be considered: material strength, dimensional parameters, actuation mechanisms, and structural configuration. We conducted a quantitative analysis of each of these aspects. The results showed that using stronger materials such as Carbon Fiber-UHMWPE or Carbon Fiber-Aluminum can increase the critical buckling load of a single module to 1,596.09 N, sufficient to support a person weighing up to approximately 162.74 kg. Similarly, increasing the bar radius to 0.794 cm (5 × the baseline) can raise the load capacity to 4,417.18 N (about 450 kg), while prestress tuning via actuation can push it to 1,002.00 N, supporting around 102.12 kg. Structural configurations, such as horizontally combined or bridge-like assemblies, can moderately enhance capacity, though they remain constrained by the load limits of individual modules. More details and analysis are provided in the "Supplementary Methods" Quantitative study of tensegrity-block load capacity.

Biological systems use manipulation capabilities to rescue individuals. For example, ants have been observed to engage in complex behaviors to assist and free trapped members of their colony[50]. The previously discussed robotic rescue scenario depicted in Fig. 5b likewise serves as an example of carrying manipulation.

In addition, manipulation in biology is not limited to animals with opposable thumbs—dolphins can play with a ball[47]. Similarly, Fig. 1e and Movie S10 show how blocks can link to form a dynamic, non-prehensile conveyor system, moving a ball (diameter: 72 cm, weight: 430 g) without the need for direct grasping. This is achieved by the synchronized movements of the connected blocks, simulating the wave motion of a surface that propels a ball. To further explore the adaptability and limitations of this conveyor system, with the same control sequence, we extended our testing to three other objects: a cylinder (perimeter: 180 cm, height: 61 cm, weight: 2050 g), an irregularly shaped bean bag cushion (max perimeter: 280 cm, height: 1 m, weight: 745 g), and a cuboid box (51 cm × 54 cm × 47cm, weight: 1712 g) as shown in Movie S10. The success rate we tested was 5/5 for both the ball and the cylinder. The cushion's success rate was lower, 4/5, due to its tendency to fall from the middle of the conveyor before reaching its destination, indicating challenges in maintaining stability for objects with shifting centers of gravity. We tried different initial orientations for the box; manipulation was successful for 2 of the 5 configurations we tried. The box's failures were attributed to one of its corners becoming lodged in the face with four strings, showing the limitations of the system's ability to handle objects with sharp edges and rigid structures.

Locomotion

Robotic locomotion uses two primary strategies. Statically stable approaches, used by e.g. Honda's ASIMO[51], maintain constant balance by keeping the center of mass above a well-defined support polygon. Dynamic gaits, utilized by e.g. Boston Dynamics robots[52], allow faster

motion, such as running or jumping, but require more sophisticated control approaches. In the paper, we focus on statically stable gaits for their simplicity and ease of control. We note, however, that lightweight robots are also well-suited to dynamic motion strategies[53].

Control and planning strategies in the literature vary, from fully pre-programmed sequences, such as Sony's dancing robots[54], to gaits generated by machine learning methods that autonomously optimize motion for diverse environments[55]. As this work focuses on robot design and capabilities, we implement an approach that sits somewhere in between. A human specifies the basic pattern as a time-dependent sequence of constraints (e.g., the left front foot should be lifted at time 2 s and the left back foot at 6 s while maintaining a maximum width profile of 0.37 m) and an automated *gait generation helper* algorithm constructs the control sequence, determining the string lengths needed to satisfy these constraints. In multi-robot setups, the *gait generation helper* treats the connected endcaps between robots as single units to ensure synchronized movement. More details about *gait generation helper* can be found in the "Supplementary Methods" and Fig. S3. For single robots, the gait is inspired by the quadrupedal "amble" pattern[56], where feet on the same side are lifted and moved forward sequentially. In multi-robot setups, the *gait generation helper* coordinates synchronized movement by treating connected endcaps between robots as single units, with feet grouped into two sets based on a zigzag pattern of diagonally adjacent feet. The *gait generation helper* algorithm adapts the control lengths to different environmental constraints, ensuring smooth and coordinated movement.

Locomotion dynamic models. To understand how slopes and surface friction impact walking behavior, we developed a dynamic locomotion model that helps explain why these differences occur and predict their effects. This model not only allows us to create a mechanical theory of locomotion but also provides a framework for testing our hypotheses through experiments. The dynamic model is based on the Lagrangian method[31] and is represented by equation $\boldsymbol{M}\ddot{\boldsymbol{n}}+\boldsymbol{D}\dot{\boldsymbol{n}}+\boldsymbol{K}\boldsymbol{n}=\boldsymbol{f}_{ex}-\boldsymbol{g}$, where $\boldsymbol{M}$, $\boldsymbol{n}$, $\boldsymbol{K}$, $\boldsymbol{D}$, $\boldsymbol{f}_{ex}$, and $\boldsymbol{g}$ are the mass, nodal coordinates, stiffness, damping, external, and gravitational matrices. The external forces $\boldsymbol{f}_{ex}$ at the contact points can be divided into parallel ($\boldsymbol{f}_{ex,\parallel}$) and perpendicular ($\boldsymbol{f}_{ex,\perp}$) components, satisfying: $\boldsymbol{f}_{ex}=\boldsymbol{f}_{ex,\parallel}+\boldsymbol{f}_{ex,\perp}$. To model how the robot interacts with the ground, we treat the ground as a spring-damper system. Assume the ith node is contacting the ground, the $\boldsymbol{f}_{exi,\perp}$ and $\boldsymbol{f}_{exi,\parallel}$ can be written as: $\boldsymbol{f}_{exi,\perp}=(K_G|n_{zi}|+C_G|\dot{n}_{zi}|)\otimes\begin{bmatrix}0 & 0 & 1\end{bmatrix}^T$ and $\boldsymbol{f}_{exi,\parallel}=\mu|\boldsymbol{f}_{exi,\perp}|\,\mathrm{sgn}\,(\dot{\boldsymbol{n}}_i-\begin{bmatrix}0 & 0 & |\dot{n}_{zi}|\end{bmatrix}^T)$, where K_G, C_G, and μ are the stiffness, damping, and friction coefficients of the ground, and sgn($\boldsymbol{v}$) is an operation that takes the direction of the vector $\boldsymbol{v}$.

To validate this model, we conducted physical experiments on three different surfaces: wood, a coir vinyl mat, and sandpaper, each at slopes of 0, 5, 10, and 15 degrees. The surfaces are modeled by adjusting only the friction coefficient in the simulator. We estimated these coefficients by tilting each surface until the robot began to slip, resulting in friction values of μ_{wood} = 0.354, μ_{coir} = 0.854, and μ_{sand} = 1.412. This method does not distinguish between kinetic and static friction coefficients. Comparisons of the simulator's output with real-world tests are shown in Fig. 8. The results show that the simulation provides a useful prediction, with the shapes of the curves for the various surfaces for the simulation qualitatively matching the curves from the experiments. The lowest friction surface (wood; red curve) has the shortest walking distances for the robot per gait cycle for all non-zero slopes in both experiment and simulation. Steeper slopes result in shorter walking distances. The discrepancies between the simulation and experimental results are primarily due to simplifications in the simulation's ground interaction model. In the simulation, we assume idealized contact geometry and uniform friction coefficients across all endcaps. However, in the real system, the four endcaps that contact the ground include two active and two passive connectors, which differ in shape, contact area. These physical differences influence how each endcap interacts with the surface, leading to behaviors not captured by the current model. In addition to this modeling limitation, other contributing factors include encoder noise or latency, minor variations in surface friction, unmodeled compliance in the mechanical structure, and asymmetries in actuator performance. Despite these sources of discrepancy, the simulation captures key trends across surfaces and slope angles, supporting its utility as a predictive tool.

Locomotion efficiency and cost of transport. To evaluate the energy efficiency of our locomotion system, we calculated the Cost of Transport (CoT), a dimensionless metric that compares energy efficiency across robotic and biological systems (the details of the calculation can be found in the "Supplementary Methods"). CoT is defined as the total energy consumed divided by the work done to move the system's weight over a given distance, i.e., $\mathrm{CoT}=\frac{E}{mgd}$, where E is energy consumption, m is mass, g is gravity, and d is the distance traveled. The results show that our module is less efficient than some of the aquatic robots, such as octopus-inspired and reconfigurable armed robots[57], but more efficient than a prior motor-driven soft six-bar tensegrity robot[58] and significantly more efficient than soft modular robots actuated by SMAs[20]. Specifically, the CoT for single-, two-, and four-module locomotion is 163, 143, and 178, respectively. The two-module configuration is the most efficient because it achieves relatively long strides while maintaining low overall power consumption and mechanical complexity. The single-module case suffers from reduced stride length and relatively high energy use per unit mass. In contrast, the four-module configuration experiences energy losses due to internal deformation, coordination overhead, and imperfect load sharing, which offset the benefits of having more actuators. Further details can be found in Fig. S7.

Outdoor locomotion demonstrations. Outdoor environments present unique challenges and opportunities for modular robot locomotion. Depending on how blocks are arranged, different locomotion strategies can be employed to navigate various terrains and obstacles. Figure 9 shows several modes of locomotion: Traversing a stream by lifting the front blocks while walking with the rear blocks on non-level dirt surfaces with leaves and stones (a, Movie S6), traversing a log tunnel (b, Movie S7) and a narrow corridor between trees (c, Movie S8) by changing shape before walking, and a "standard" locomotion gait (d, Movie S2, Table S6) with speed measurements across grass, soil, asphalt, snow, and ice. For traversing narrow alleys and tunnels, the same gait is employed but with different directional constraints to accommodate the specific environments. In tunnels, the primary constraint is the height (z-coordinate), which must remain below a certain threshold to avoid collisions with the tunnel ceiling. Narrow alleys limit the robot's maximum width during the gait. From the experimental results, the two-block system is the fastest for all terrains except in the snow scenario, where the four-block system is the fastest. We surmise that the single-block system is slow because only a single foot is lifted at a time, leaving the other three feet down to form a support triangle. For the four-block system, the problem is the opposite – when lifting all diagonal feet in a zigzag pattern, more feet are left on the ground to permit perfect compliance to the surface; some of the "ground" feet are in fact slightly lifted and slip. Different gaits or lower-level control of the compliance of feet to the surface might enable faster locomotion for multi-block systems.

Discussion

Existing modular robot systems have demonstrated the ability to use simple components to achieve a variety of tasks[6,10]. However, they have

https://doi.org/10.1038/s41467-025-60982-0

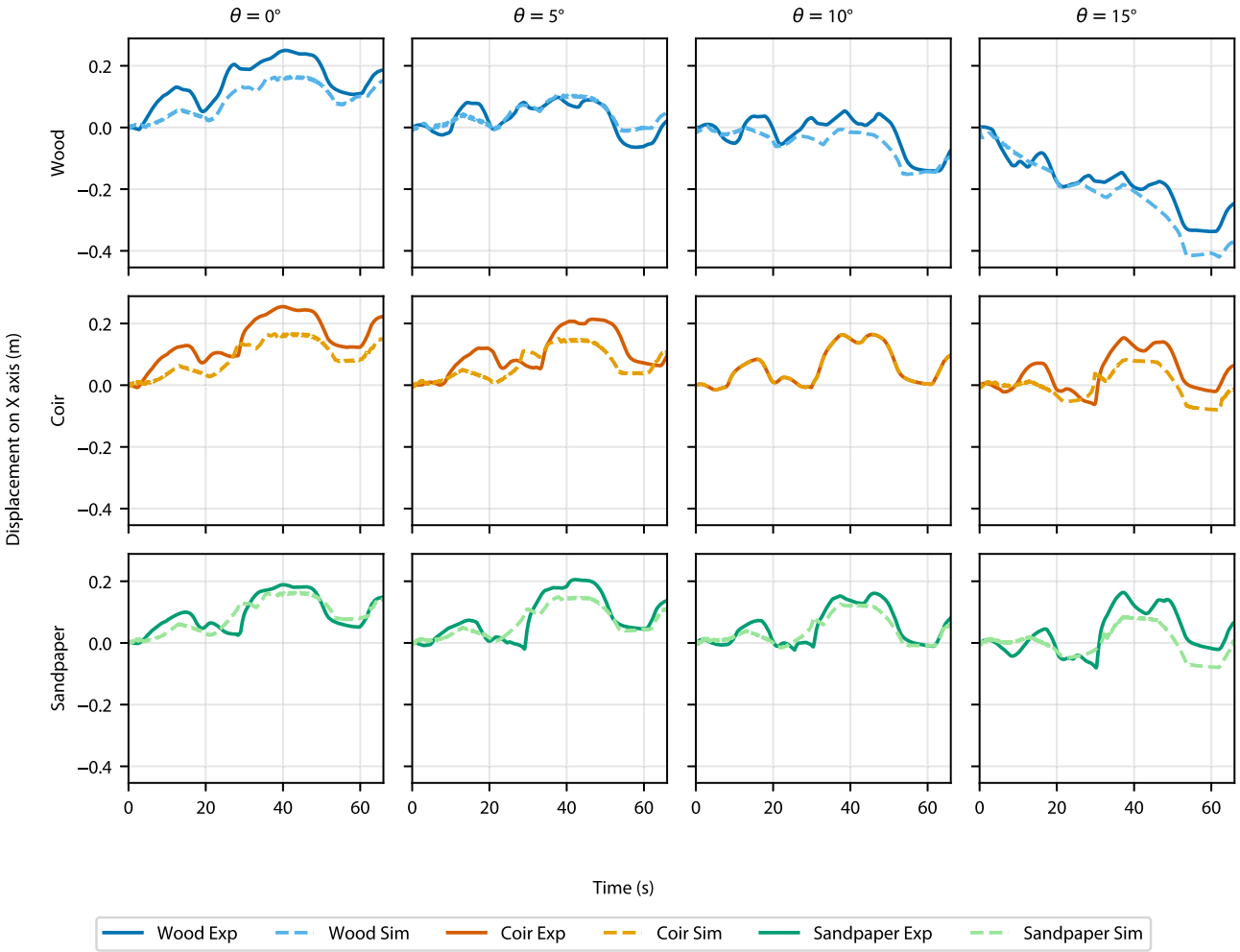

Fig. 8 | The historical data for the upper node's *x*-coordinate across various surfaces (wood in red, coir vinyl in orange, and sandpaper in blue) and slope angles are presented as follows. From left to right, slope angles are $\theta = 0°$, $\theta = 5°$, $\theta = 10°$, and $\theta = 15°$, respectively.

been primarily limited to locomotion and manipulation tasks[6], lacking the deployability and the capability to build 3D temporary infrastructures. Our study bridges this gap by integrating the principles of tensegrity—characterized by inherent lightweight and deformable properties—into modular blocks, enabling the robots to combine three critical functions within a single design: navigating challenging terrains, performing complex manipulation tasks, and constructing temporary structures with real-world applications.

The mechanical design incorporates eight rods linked by flexible joints and is complemented by active connectors on the endcaps, facilitating 3D structure formation and whole-body deformation, improving manipulation and locomotion in unstructured outdoor environments. Transitioning from indoor to outdoor applications highlighted several environmental challenges, such as fluctuating temperatures affecting battery life and low light conditions impairing state estimation. These issues, coupled with the challenges of navigating diverse terrains like rugged woodland, underscore the need for more robust and adaptive gait optimization strategies for modular systems. Additionally, adverse weather conditions such as strong winds or snowstorms can impact vertical lifting and aerial assembly. We have conducted experiments in strong winds, during which both the drone and the robot experienced noticeable swaying, making it difficult to maintain precise control. Under more extreme conditions, drone-based vertical assembly may become infeasible. Therefore, environmental parameters—such as wind speed, temperature, and snow depth—must be carefully evaluated before deployment, with fallback plans including postponing or relocating the operation.

The deployment system, assisted by rotorcraft, enables the rapid assembly of large-scale 3D structures. However, our experiments indicate that further system refinements are needed to handle a larger array of robotic modules and more dynamic tasks. A key limitation of the current approach is the reliance on a drone-mounted camera for global state estimation and centralized gait planning, which limits autonomy and scalability. To overcome this, future work could explore equipping each module with onboard cameras, depth sensors, or infrared/LiDAR-based proximity sensors for local perception, similar to the approaches demonstrated by Daudelin et al.[59]. Additionally, ultra-wideband (UWB) localization systems could provide low-latency relative positioning among modules, enabling local coordination without the need for global vision. Sensor fusion with IMUs would further improve robustness in unstructured or outdoor environments. These sensing capabilities would support decentralized gait planning and coordination, potentially using pre-learned motion libraries or onboard reinforcement learning. Such advances would reduce dependence on external infrastructure and enable fully autonomous operation in GPS-denied, cluttered, or remote environments.

Due to their deformability, tensegrity structures excel at shock absorption, making them well-suited for outdoor applications; however, this comes with a trade-off in load-bearing capacity. The optimal choice depends on the specific scenarios in which our robots are

https://doi.org/10.1038/s41467-025-60982-0

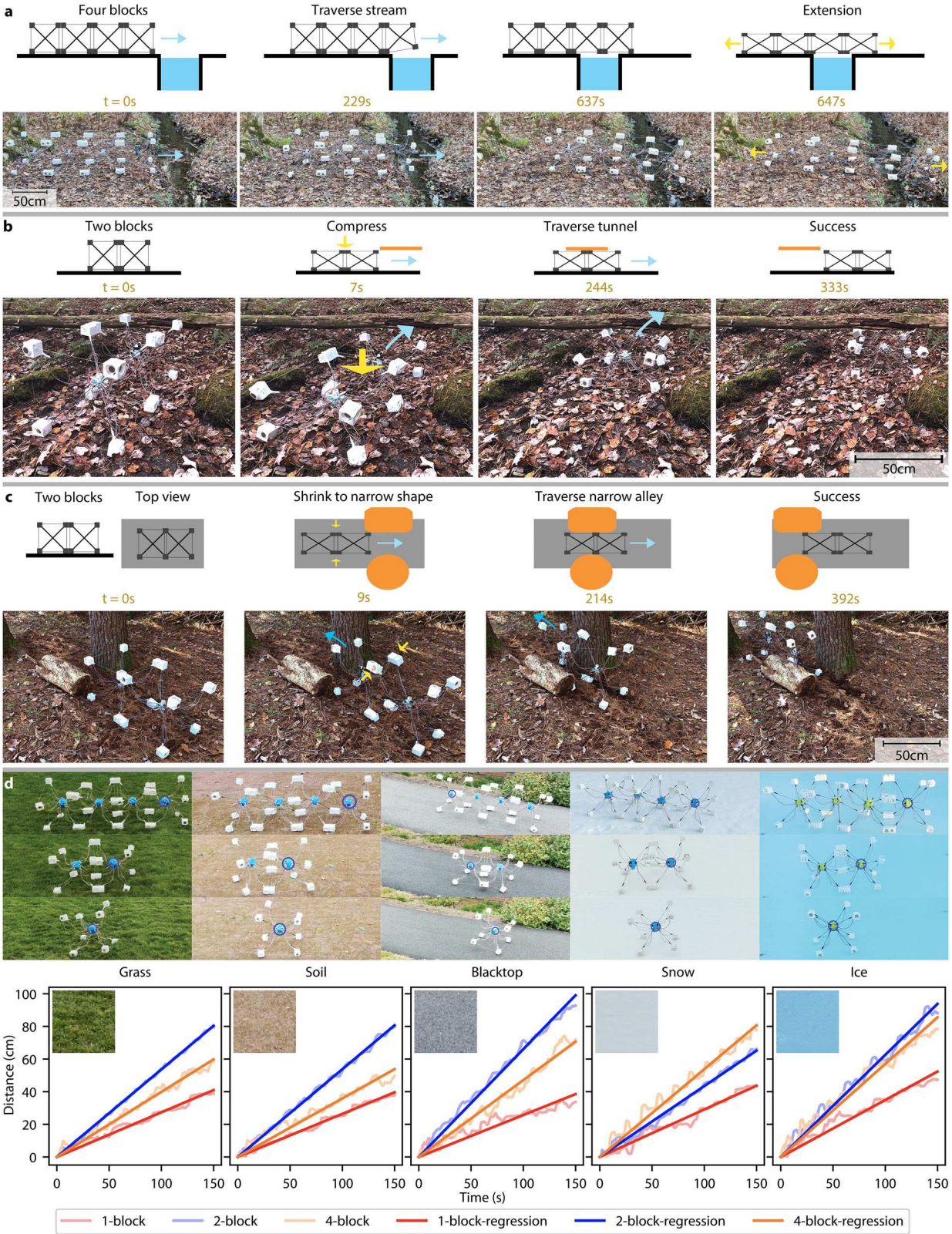

Fig. 9 | Locomotion in natural environments. a Four blocks cross a 0.6 m wide stream, indicated by a blue arrow, forming a bridge, shown by a yellow arrow (t = 647 s). **b** Two blocks compress vertically to pass under a log tunnel (0.35 m high) from their original height (0.52 m) and then traverse (t = 244 s). **c** To navigate a narrow alley (0.37 m wide), the blocks compress horizontally. **d** Speed comparison for different block numbers on grass, soil, blacktop, snow, and ice, with linear regression estimating speeds for each configuration.

deployed. In locations where rotorcraft deployment is the only option, we would select robots better suited for shock absorption. However, in situations that require heavy loading capacity, we might need to compromise on shock absorption. In such cases, adjusting the stiffness of the cables can help make them softer, allowing the structure to maintain some level of shock absorption ability while meeting the heavy loading requirements. A related consideration is the system's ability to survive drop impacts during aerial deployment. Our experiments indicate that a 3-meter drop is a reliable operational threshold across various ground conditions. However, beyond this height, the carbon fiber rods become the primary point of failure due to limitations in flexural strength, often fracturing under excessive bending moments. To improve drop survivability for higher altitudes, several hardware enhancements can be considered. These include replacing carbon fiber with thicker or higher-strength composites, using reinforced or metallic endcaps to reduce brittle failure, and upgrading strings to more durable, high-tensile materials (more details in "Supplementary methods" Quantitative study of tensegrity-block load capacity).

We identified several critical failure modes that impact the reliability of modular tensegrity systems across mechanical, electrical, software, and functional domains. Mechanically, carbon fiber components are the most vulnerable under high loads or impacts, and cables can wear over time, leading to eventual breakage. When multiple robots are connected, unequal tension distribution can overload individual motors, occasionally damaging gearboxes. Electrically, power spikes from motor overloading can cause PCB overheating, which can be mitigated through better power monitoring and power management hardware. Software failures mainly stem from computer vision issues under inconsistent lighting, currently addressed through manual calibration. Functionally, physical debris—like sand or small stones—can block inter-module connections. Enlarging endcaps and increasing latch gap tolerances may improve resilience in outdoor environments. Addressing these failure modes through improved materials, electronics, and design adjustments will be essential for ensuring long-term robustness in real-world deployments.

Another promising direction is improving the adaptability of the non-prehensile manipulation system through sensory feedback. Currently, synchronized gaits are executed in open-loop to move objects across the conveyor-like surface formed by multiple modules. While effective for simple objects like spheres and cylinders, irregular shapes can cause failures during transitions between modules. We envision integrating computer vision using the existing drone-mounted overhead camera to track the object's position in real time. This would enable a closed-loop control scheme where, if an object fails to move from one module to the next, the system could repeat or adjust motion patterns until success is detected. This feedback mechanism would significantly enhance robustness and adaptability, particularly in unstructured environments.

Our research provides a starting point for exploring the use of modular robots in building temporary active structures intended for human use. Inspired by the cooperative behaviors of insect swarms, this study demonstrates the potential of simple, modular units to collaboratively construct functional setups like emergency shelters without complex control systems. The insights from our experiments suggest practical avenues for further development, particularly in enhancing the structural integrity and deployment efficiency of these systems. For instance, a modular-assembled tent structure successfully housed an adult, showcasing its immediate utility. However, other configurations, such as bridges assembled with four modules and stretchers transported by two modules, though effective for specific tasks, currently lack the strength to support human weight.

Looking ahead, several key research directions could further advance the capabilities of modular tensegrity robotic systems. On the practical side, efforts could focus on developing robots that are not only rapidly deployable but also structurally robust enough for real-world tasks such as infrastructure construction—bridges, shelters, and support platforms. Improving load-bearing capacity and enabling adaptive load distribution through multi-module cooperation will be critical for these applications. In parallel, introducing additional degrees of freedom at the connector joints—such as ball joint mechanisms—could allow modules to achieve more versatile shape adaptation. From an autonomy perspective, the goal is to enable fully autonomous deployment in unstructured or hard-to-reach environments. This would involve integrating onboard sensors, decentralized control strategies, and real-time motion planning. We see strong potential in using reinforcement learning (RL) and model predictive control (MPC) to make gait generation and connection strategies more adaptive to terrain variation and sensor feedback. For example, RL policies trained in simulation using reward functions that encode stability, energy efficiency, and forward progress could be transferred to hardware via sim-to-real strategies such as domain randomization. MPC could complement this by using onboard state estimation and predictive models to optimize joint trajectories in real time under physical constraints. Together, these methods would allow the robot to dynamically adjust to unpredictable terrain, improve reliability, and recover from disturbances.

Furthermore, the modular and distributed nature of our system makes it well-suited for swarm robotics. Future work could explore collaborative behaviors in which multiple modules share state variables, such as position, connection status, or actuator load, via low-bandwidth protocols. Using decentralized strategies such as consensus-based control or local behavior rules, modules could coordinate locomotion and assembly tasks in a scalable and fault-tolerant manner. This type of distributed decision-making would enhance robustness and adaptability, particularly in large-scale or dynamic environments. Taken together, these directions could push modular tensegrity systems toward more intelligent, autonomous, and field-ready applications. We anticipate that modular shape-changing lightweight blocks will enhance multi-functional robotics, supporting applications such as automated infrastructure construction with integrated structural and actuation elements, compact building blocks for space systems, and deeper insights into biological systems to drive bio-inspired robotics design.

Methods

Block fabrication and design

Each block consists of a flexible central joint, eight magnetic endcaps, and a Printed Circuit Board (PCB). The central joint is a flexible core of the robot, fabricated from Thermoplastic Polyurethane (TPU) material (1.75 mm, Amazon Basics), selected for a combination of flexibility and durability. The central core features an internal cavity sized to house a battery (21,700 3.7 V 4200 mAh). Carbon fiber rods (diameter = 3.5 mm; length = 30 cm) were chosen for their high strength-to-weight ratio.

We created two designs for robot endcaps: 2A1P and 1A2P. The 2A1P type comprises two active and one passive connector, whereas the 1A2P type consists of one active and two passive connectors. These endcaps provide structural support for multi-block assemblies and house the motors. Each 2A1P endcap holds two servo motors for locking and unlocking connections and one primary motor for controlling string lengths. For weight balance, the 1A2P type contains one servo motor and two primary motors. The primary motor is an N20 DC motor with a magnetic encoder (12V/30,000 rpm with a 1:298 gear ratio); servo motors are a micro 3.7g servo. Two different sizes of magnets are used in the design: for the active connector, a magnet with the N pole facing outward (Amazing Magnets, product number D063J-N42, thickness: 1.59 mm, diameter: 31.75 mm), and for the passive connector, a magnet with the S pole facing outward (Amazing Magnets, product number D125J-N42, thickness: 3.18 mm, diameter: 31.75 mm).

The PCB, detailed in Fig. S1, is a six-layer design with a Wi-Fi module, one microcontroller for control commands and sensor data, a second microcontroller for actuation signals, an inertial measurement unit, and temperature sensors.

Experimental design and data analysis

This section presents the experimental design and data analysis approaches utilized to evaluate the performance of robotic modules in locomotion and rotorcraft-based state estimation experiments across different outdoor terrains, employing tracking and computer vision techniques for measurement and analysis.

For the drop test, we tested the block on four different surfaces (Movie S12): hard-packed snow (tensile strength ranging from 0.1 to 1 MPa[60]), grass-covered soil (stiffness from 240 to 1693 kN/m[61]), hard-packed gravel (stiffness modulus from 126 to 426 MPa[62]), and soil (stiffness from 3 to 22.1 MN/m[63]). To conduct the test, we first used a rotorcraft to grasp the robot from the ground, recording the initial height. The rotorcraft then ascended 3 meters above this height before releasing the robot.

For experiments testing the compressive and tensile properties of a block with a half-meter width, we developed a customized test platform according to standard testing protocols, as shown in Fig. S6. In the compression test, a wooden platform was horizontally suspended by strings attached to each corner, which were tension-adjusted to ensure planarity, with a level used to verify horizontality. The load was incrementally increased by filling a centrally placed bucket with sand (each time 500 g), while a vernier caliper attached to the left T-slots of the support frame measured displacement. A counterweight system was employed to establish an initial load of zero, using a second bucket pre-filled with a calculated amount of sand, connected via a twin-pulley system to balance the weight of the empty bucket and platform. For the tensile test, the module was suspended by a central string that passed through a freely sliding connector within the frame's T-slots to ensure vertical alignment, confirmed with a mounted level. Four equal-length strings were attached to the endcaps on the right face of the module, converging into a single strand that anchored to the right T-slots. Similarly, four strings connected to the left endcaps were merged and routed through a pulley to a bucket, which was gradually filled with sand to increase the load.

In the alignment experiment (see Fig. 4d), a paper with grids representing various angles was glued on the ground. We fixed the left block in position and manually positioned the right block to achieve specific initial positions and angles. For each angle, we conducted at least three tests at different positions and used the median value for the final results. Our locomotion experiments were conducted outdoors across a variety of terrains to evaluate the performance of different robotic modules. To quantify the speed of each module on different surfaces, we recorded their movements using a camera system. The robots' central joints were distinctly marked with blue/green tape to facilitate tracking during video analysis.

For accurate distance measurement and speed calculation, we equipped the testing area with boards featuring AprilTags[64] within the camera's field of view. These served as reference points, enabling us to employ computer vision techniques to track the trajectory of the central joints of the blocks. The resulting plots illustrating the distance-time relationship are presented in Fig. 9 and Movie S2, where the speed is indicated by the slope of the linear regression. For consistency in multi-block locomotion experiments, we track the first block relative to the direction of movement in all cases.

Rotorcraft-camera state estimation experiments were consistently performed over soil interspersed with small stones, vegetation, or snow. We utilized the DJI Matrice 350 RTK rotorcraft. The rotorcraft was maneuvered to a fixed position at a height of 4.5 m and was equipped with its default camera to capture images at a frequency of 30 Hz. We used a Rybozen 4K audio-video capture card to connect the laptop to the remote controller for image transmission. These images with a resolution of 2560×1440 pixels were then utilized for state estimation purposes.

Outdoor structure formation with a rotorcraft includes the construction of bridges, tents, and actuatable scaffolding. An operator manually piloted the rotorcraft using a remote controller. Bridge constructions and actuatable scaffolding were erected over a soil environment, whereas the tent formation was carried out on grass partially covered with snow.

To classify how each gait affected the displacement and orientation of a block, 25 trials were conducted for each gait to measure the expected results. The resulting net translation and rotation for each trial are illustrated in Fig. S2, where 5 outliers for each gait are removed. The mean displacement values among 20 trials for each gait are used for planning.

Data availability

All data needed to evaluate the conclusions in the paper are present in the paper or the Supplementary Materials.

References

1. Engelberger, J. F. *Robotics in practice: management and applications of industrial robots* (Springer Science & Business Media, New York, NY, 2012).
2. Reid, C. R. et al. Army ants dynamically adjust living bridges in response to a cost–benefit trade-off. *Proc. Natl. Acad. Sci.* **112**, 15113–15118 (2015).
3. Murata, S. & Kurokawa, H.*Self-organizing robots*, vol. 77 (Springer, Tokyo, 2012).
4. Parker, L. E., Rus, D. & Sukhatme, G. S. Multiple mobile robot systems. *Springer handbook of robotics* 1335–1384 (2016).
5. Yim, M. et al. Modular self-reconfigurable robot systems [grand challenges of robotics]. *IEEE Robot. Autom. Mag.* **14**, 43–52 (2007).
6. Liang, G., Wu, D., Tu, Y. & Lam, T. L. Decoding modular reconfigurable robots: A survey on mechanisms and design. *Int. J. Robot. Res.* **44**, 740–767 (2025).
7. Liu, C., Whitzer, M. & Yim, M. A distributed reconfiguration planning algorithm for modular robots. *IEEE Robot. Autom. Lett.* **4**, 4231–4238 (2019).
8. Jing, G., Tosun, T., Yim, M. & Kress-Gazit, H. An end-to-end system for accomplishing tasks with modular robots. In *Proceedings of Robotics: Science and Systems* (2016).
9. Wei, H., Cai, Y., Li, H., Li, D. & Wang, T. Sambot: A self-assembly modular robot for swarm robot. In *2010 IEEE International Conference on Robotics and Automation*, 66–71 (2010).
10. Ozkan-Aydin, Y. & Goldman, D. I. Self-reconfigurable multilegged robot swarms collectively accomplish challenging terradynamic tasks. *Sci. Robot.* **6**, eabf1628 (2021).
11. Zhang, C., Zhu, P., Lin, Y., Jiao, Z. & Zou, J. Modular soft robotics: Modular units, connection mechanisms, and applications. *Adv. Intell. Syst.* **2**, 1900166 (2020).
12. Sugihara, J., Nishio, T., Nagato, K., Nakao, M. & Zhao, M. Design, control, and motion strategy of trady: Tilted-rotor-equipped aerial robot with autonomous in-flight assembly and disassembly ability. *Adv. Intell. Syst.* **5**, 2300191 (2023).
13. Tu, Y., Liang, G. & Lam, T. L. Freesn: A freeform strut-node structured modular self-reconfigurable robot - design and implementation. In *2022 International Conference on Robotics and Automation (ICRA)*, 4239–4245 (2022).
14. Skelton, R. E. & De Oliveira, M. C.*Tensegrity Systems*, vol. 1 (Springer, 2009).
15. Paul, C., Valero-Cuevas, F. & Lipson, H. Design and control of tensegrity robots for locomotion. *IEEE Trans. Robot.* **22**, 944–957 (2006).

16. Bruce, J. et al. SUPERball: Exploring tensegrities for planetary probes. In *12th International Symposium on Artificial Intelligence, Robotics and Automation in Space (i-SAIRAS)* https://ntrs.nasa.gov/search.jsp?R=20190001649 (2014).
17. Kobayashi, R., Nabae, H., Endo, G. & Suzumori, K. Soft tensegrity robot driven by thin artificial muscles for the exploration of unknown spatial configurations. *IEEE Robot. Autom. Lett.* **7**, 5349–5356 (2022).
18. Zappetti, D., Mintchev, S., Shintake, J. & Floreano, D. Bio-inspired tensegrity soft modular robots. In *Biomimetic and Biohybrid Systems*, 497–508 (Springer, 2017).
19. Zhao, L. et al. Soft lattice modules that behave independently and collectively. *IEEE Robot. Autom. Lett.* **7**, 5942–5949 (2022).
20. Zhao, L. et al. Starblocks: Soft actuated self-connecting blocks for building deformable lattice structures. *IEEE Robot. Autom. Lett.* **8**, 4521–4528 (2023).
21. Ceron, S., Kimmel, M. A., Nilles, A. & Petersen, K. Soft robotic oscillators with strain-based coordination. *IEEE Robot. Autom. Lett.* **6**, 7557–7563 (2021).
22. Malley, M., Haghighat, B., Houel, L. & Nagpal, R. Eciton robotica: Design and algorithms for an adaptive self-assembling soft robot collective. In *2020 IEEE International Conference on Robotics and Automation (ICRA)*, 4565–4571 (2020).
23. Li, S. et al. Scaling up soft robotics: A meter-scale, modular, and reconfigurable soft robotic system. *Soft Robot.* **9**, 324–336 (2022).
24. Usevitch, N. S. et al. An untethered isoperimetric soft robot. *Sci. Robot.* **5**, eaaz0492 (2020).
25. Spinos, A., Carroll, D., Kientz, T. & Yim, M. Variable topology truss: Design and analysis. In *2017 IEEE/RSJ International Conference on Intelligent Robots and Systems (IROS)*, 2717–2722 (2017).
26. Werfel, J., Petersen, K. & Nagpal, R. Designing collective behavior in a termite-inspired robot construction team. *Science* **343**, 754–758 (2014).
27. Gregg, C. E. et al. Ultralight, strong, and self-reprogrammable mechanical metamaterials. *Sci. Robot.* **9**, eadi2746 (2024).
28. Goessens, S., Mueller, C. & Latteur, P. Feasibility study for drone-based masonry construction of real-scale structures. *Autom. Constr.* **94**, 458–480 (2018).
29. Augugliaro, F. et al. The flight assembled architecture installation: Cooperative construction with flying machines. *IEEE Control Syst. Mag.* **34**, 46–64 (2014).
30. Chin, L., Burns, M., Xie, G. & Rus, D. Flipper-style locomotion through strong expanding modular robots. *IEEE Robot. Autom. Lett.* **8**, 528–535 (2023).
31. Ma, S., Chen, M. & Skelton, R. E. Tensegrity system dynamics based on finite element method. *Composite Struct.* **280**, 114838 (2022).
32. Chen, M. et al. Energy-efficient cable-actuation strategies of the v-expander tensegrity structure subjected to five shape changes. *Mech. Res. Commun.* **127**, 104026 (2023).
33. Mintchev, S. et al. An underwater reconfigurable robot with bioinspired electric sense. In *2012 IEEE International Conference on Robotics and Automation*, 1149–1154 (2012).
34. Kurumaya, S. et al. A modular soft robotic wrist for underwater manipulation. *Soft Robot.* **5**, 399–409 (2018).
35. Ze, Q. et al. Soft robotic origami crawler. *Sci. Adv.* **8**, eabm7834 (2022).
36. Robertson, M. A. & Paik, J. New soft robots really suck: Vacuum-powered systems empower diverse capabilities. *Sci. Robot.* **2**, eaan6357 (2017).
37. Kwok, S. W. et al. Magnetic assembly of soft robots with hard components. *Adv. Funct. Mater.* **24**, 2180–2187 (2014).
38. Onal, C. D. & Rus, D. A modular approach to soft robots. In *2012 4th IEEE RAS EMBS International Conference on Biomedical Robotics and Biomechatronics (BioRob)*, 1038–1045 (2012).
39. Lee, J.-Y., Kim, W.-B., Choi, W.-Y. & Cho, K.-J. Soft robotic blocks: Introducing sobl, a fast-build modularized design block. *IEEE Robot. Autom. Mag.* **23**, 30–41 (2016).
40. Vergara, A., Lau, Y.-S., Mendoza-Garcia, R.-F. & Zagal, J. C. Soft modular robotic cubes: Toward replicating morphogenetic movements of the embryo. *PLoS One* **12**, e0169179 (2017).
41. Zou, J., Lin, Y., Ji, C. & Yang, H. A reconfigurable omnidirectional soft robot based on caterpillar locomotion. *Soft Robot.* **5**, 164–174 (2018).
42. Romanishin, J. W., Gilpin, K. & Rus, D. M-blocks: Momentum-driven, magnetic modular robots. In *2013 IEEE/RSJ International Conference on Intelligent Robots and Systems*, 4288–4295 (2013).
43. Kotay, K., Rus, D., Vona, M. & McGray, C. The self-reconfiguring robotic molecule. In *Proceedings. 1998 IEEE International Conference on Robotics and Automation*, vol. 1, 424–431 (1998).
44. Tosun, T., Davey, J., Liu, C. & Yim, M. Design and characterization of the ep-face connector. In *2016 IEEE/RSJ International Conference on Intelligent Robots and Systems (IROS)*, 45–51 (2016).
45. Khaled, M. S. et al. Tensegrity laboratory drilling rig for earth and space drilling, mining, and exploration. *Int. J. Solids Struct.* **252**, 111785 (2022).
46. Parker, S. T. & Gibson, K. R. Object manipulation, tool use and sensorimotor intelligence as feeding adaptations in cebus monkeys and great apes. *J. Hum. Evolut.* **6**, 623–641 (1977).
47. Delfour, F., Faulkner, C. & Carter, T. Object manipulation and play behaviour in bottlenose dolphins (tursiops truncatus) under human care. *Int. J. Comp. Psychol.* **30**, 32968 (2017).
48. Feinerman, O., Pinkoviezky, I., Gelblum, A., Fonio, E. & Gov, N. S. The physics of cooperative transport in groups of ants. *Nat. Phys.* **14**, 683–693 (2018).
49. Barros, R. J. F., Silva Filho, J. L. P., Neto, J. V. S. & Nascimento, T. P. An open-design warehouse mobile robot. In *2020 Latin American Robotics Symposium (LARS), 2020 Brazilian Symposium on Robotics (SBR) and 2020 Workshop on Robotics in Education (WRE)*, 1–6 (2020).
50. Miler, K. & Turza, F. "o sister, where art thou?"—a review on rescue of imperiled individuals in ants. *Biology* **10**, 1079 (2021).
51. Kim, S. & Wensing, P. Design of dynamic legged robots. *Found. Trends Robot.* **5**, 117–190 (2017).
52. Bhatti, J., Plummer, A. R., Iravani, P. & Ding, B. A survey of dynamic robot legged locomotion. In *2015 International Conference on Fluid Power and Mechatronics (FPM)*, 770–775 (2015).
53. Calisti, M., Picardi, G. & Laschi, C. Fundamentals of soft robot locomotion. *J. R. Soc. Interface* **14**, 20170101 (2017).
54. Or, J. Towards the development of emotional dancing humanoid robots. *Int. J. Soc. Robot.* **1**, 367–382 (2009).
55. Tsounis, V., Alge, M., Lee, J., Farshidian, F. & Hutter, M. Deepgait: Planning and control of quadrupedal gaits using deep reinforcement learning. *IEEE Robot. Autom. Lett.* **5**, 3699–3706 (2020).
56. Carr, B. J. & Dycus, D. Canine gait analysis. *Today's. Vet. Pract.* **6**, 93–98 (2016).
57. White, C. H., Lauder, G. V. & Bart-Smith, H. Tunabot flex: A tuna-inspired robot with body flexibility improves high-performance swimming. *Bioinspiration Biomim.* **16**, 026019 (2021).
58. Rieffel, J. & Mouret, J.-B. Adaptive and resilient soft tensegrity robots. *Soft Robotics* **5**, 318–329 (2018).
59. Daudelin, J. et al. An integrated system for perception-driven autonomy with modular robots. *Sci. Robot.* **3**, eaat4983 (2018).
60. Petrovic, J. Review mechanical properties of ice and snow. *J. Mater. Sci.* **38**, 1–6 (2003).
61. Schramel, J. & Peham, C. Mechanical properties of a grass surface in the course of a year. *Equine Vet. J.* **48**, 18–18 (2016).
62. Lubis, A., Muis, Z. & Iskandar, T. The study of stiffness modulus values for ac-wc pavement. *IOP Conf. Ser. Mater. Sci. Eng.* **309**, 012113 (2018).

63. Fiedler, S., Nelson, C., Berkman, E. & DiMillio, A. Soil stiffness gauge for soil compaction control. *Public Roads* **61**, 5–10 (1998).
64. Olson, E. Apriltag: A robust and flexible visual fiducial system. In *2011 IEEE International Conference on Robotics and Automation*, 3400–3407 (2011).

Acknowledgements

We thank R. Kramer-Bottiglio, J. Booth, X. Huang, S. Lu, E. Osegueda, for helpful discussion; A. Quattrini Li, and M. Jeong for equipment support. This work was supported by the National Science Foundation (NSF): Robust Assembly of Compliant Modular Robots (Award 1954882, to DB).

Author contributions

Conceptualization: L.Z., Y.J., M.C., D.B., K.B.; Methodology: L.Z., Y.J., D.B., M.C.; Investigation: L.Z., D.B., Y.J., K.B., M.C.; Visualization: L.Z., Y.J., M.C.; Experiments Design and Implementation: L.Z., Y.J., D.B., M.C.; System Design and Implementation: L.Z., Y.J., D.B., K.B., M.C.; Algorithm Design and Implementation: L.Z., Y.J., D.B., M.C.; Funding acquisition: D.B., K.B.; Project administration: D.B., L.Z.; Supervision: D.B., K.B., M.C.; Writing: original draft: L.Z.; Writing: review & editing: L.Z., Y.J., D.B., K.B., M.C.

Competing interests

The authors declare no competing interests.

Additional information

Supplementary information The online version contains supplementary material available at https://doi.org/10.1038/s41467-025-60982-0.

Correspondence and requests for materials should be addressed to Luyang Zhao.

Peer review information *Nature Communications* thanks Priyanka Bhovad, and the other, anonymous, reviewer(s) for their contribution to the peer review of this work. A peer review file is available.